Research Article | Vol. 31, No. 25 / 4 Dec 2023 / Optics Express 41202
Optics EXPRESS

Bond-selective full-field optical coherence tomography

HAONAN ZONG,[1] CELALETTIN YURDAKUL,[1] JIAN ZHAO,[1,2] ZIAN WANG,[3] FUKAI CHEN,[4] M. SELIM ÜNLÜ,[1,3] AND JI-XIN CHENG[1,3,*]

[1]*Department of Electrical and Computer Engineering, Boston University, Boston, MA, 02215, USA*
[2]*Current Affiliation: The Picower Institute for Learning and Memory, Massachusetts Institute of Technology, Cambridge, MA 02142, USA*
[3]*Department of Biomedical Engineering, Boston University, Boston, MA 02215, USA*
[4]*Department of Biology, Boston University, Boston, MA 02215, USA*
[*]*jxcheng@bu.edu*

Abstract: Optical coherence tomography (OCT) is a label-free, non-invasive 3D imaging tool widely used in both biological research and clinical diagnosis. Conventional OCT modalities can only visualize specimen tomography without chemical information. Here, we report a bond-selective full-field OCT (BS-FF-OCT), in which a pulsed mid-infrared laser is used to modulate the OCT signal through the photothermal effect, achieving label-free bond-selective 3D sectioned imaging of highly scattering samples. We first demonstrate BS-FF-OCT imaging of 1 μm PMMA beads embedded in agarose gel. Next, we show 3D hyperspectral imaging of up to 75 μm of polypropylene fiber mattress from a standard surgical mask. We then demonstrate BS-FF-OCT imaging on biological samples, including cancer cell spheroids and *C. elegans*. Using an alternative pulse timing configuration, we finally demonstrate the capability of BS-FF-OCT on imaging a highly scattering myelinated axons region in a mouse brain tissue slice.

1. Introduction

Since the first report by Huang *et al.* in 1991, optical coherence tomography (OCT) has experienced many advanced technical developments and demonstrated significant applications in the past decades [1]. OCT has evolved from time-domain OCT (TD-OCT) [2], which mechanically scans the optical phase of the reference arm to obtain the signal from different depths, to spectral-domain/Fourier-domain OCT (SD/FD-OCT) [3–5], which spectrally resolves the detected interferometric signal from different depths without mechanically scanning. SD/FD-OCT has dramatically improved the sensitivity and imaging speed of OCT and achieved in vivo retinal imaging [4] till video rate [5]. Besides improving the scanning speed of scanning mode OCT, an alternative approach is to use multi-pixel detectors. To enable high-resolution en-face OCT imaging, time-domain full-field OCT (FF-OCT) was developed [6,7]. FF-OCT adopts wide-field illumination and a multi-pixel detector (a CCD or CMOS camera) to obtain en-face images at a given depth without scanning across the sample. FF-OCT was applied to in vivo human corneal [8] and retinal imaging [9] for ophthalmic diagnosis. FF-OCT was also used for histological imaging of different types of tissues, such as human skin tissue [10], breast tissue [11], and brain tissue [12], for cancer diagnosis. However, those conventional FF-OCT modalities can only provide tomography images without any molecular information, which limits their potential applications to samples that have different chemical compositions but similar morphology.

Vibrational microscopy has been a widely used tool for label-free molecular imaging without sample perturbation [13]. In these techniques, Raman scattering, or linear infrared absorption, is measured to provide contrast. More recently, the relatively weak signal and low acquisition speed of the spontaneous Raman scattering [14] have been boosted by coherence Raman

#503861 https://doi.org/10.1364/OE.503861
Journal © 2023 Received 29 Aug 2023; revised 9 Nov 2023; accepted 10 Nov 2023; published 21 Nov 2023

Optics EXPRESS

scattering microscopy [15,16]. Compared to Raman scattering, which has an extremely small cross-section (~10^{-30} to10^{-28} cm^2), linear infrared (IR) absorption has ten orders of magnitude larger cross-section (~10^{-18} cm^2). Despite the large cross-section, conventional IR imaging technique such as Fourier transform infrared (FTIR) [17,18] has poor spatial resolution due to the long illumination wavelength. To break this limitation, mid-infrared photothermal (MIP) microscopy, which indirectly measures IR absorption by using the photothermal effect, was developed recently [19,20]. Since then, MIP microscopy has evolved from point-scan [19–26] to wide-field configurations [27–38]. As reviewed recently [39,40], MIP microscopy offers a few advantages. First, sub-micron spatial resolution is achieved through the visible probe beam. Second, wide-field MIP microscopy enables high-throughput chemical imaging by exploiting the advantage that linear IR absorption doesn't require a tight focus. By using wide-field illumination and detection configuration, the imaging speed could reach half of the camera frame rate. Third, volumetric chemical imaging is possible through mid-infrared photothermal phase tomography [32,33,37]. Despite these advances, phase tomography, including optical diffraction tomography [32] and intensity diffraction tomography [37], is limited to weakly scattering samples and can't be applied to highly scattering specimens such as tissues.

Functional OCT modalities have been developed to add additional contrast to conventional OCT. For example, polarization OCT [41] can detect specific tissue types that can induce polarization change, spectroscopic OCT [42] measures the spectral features within the wavelength range of the OCT light source, and thermo-elastic OCT [43,44] and photothermal OCT [45–56] can obtain the absorption spectrum by measuring the photothermal effect. Photothermal OCT has been a powerful functional extension of conventional OCT since it was first demonstrated by Adler, D.C. et al. in 2008 [45]. Photothermal OCT is realized by adding another modulated heating beam to the conventional OCT, and it measures the modulation of the conventional OCT signal induced by the heating beam. Firstly, it solves the inherent difficulty of OCT, or any other direct scattering-based measurement methods, distinguishing scattering and absorption. Secondly, it provides molecular specificity to OCT by only detecting signals from specific absorbers at the heating wavelength, which can be endogenous pigments [46–48] originally existing in the sample, exogenous contrast agents [45,49–54] that are imported into the sample, or overtone absorption of non-pigment endogenous chemical components [56]. Yet, these current photothermal OCT configurations are mainly using a heating wavelength in the visible and near-infrared range, where the intrinsic absorption of biological samples is rare, which limits its wider applications. The absorption in the mid-infrared (MIR) range is more common and can provide more molecular information, which hasn't been adopted in photothermal OCT. Although there are conventional OCT modalities using MIR light sources to improve penetration depth [57], or a time-gated method to detect the reflection of MIR light from different depths [58], compared to the potential of MIR photothermal OCT, these techniques have the intrinsic MIR resolution limitation and no specificity to the absorbing molecules.

In this work, we report bond-selective full-field optical coherence tomography (BS-FF-OCT), in which a pulsed MIR laser modulates the full-field OCT signal through the photothermal effect. Our technique enables label-free bond-selective 3D sectioning imaging of highly scattering thick samples. To achieve this, we integrate a modulated MIR heating beam into a time-domain FF-OCT. We use a broadband light-emitting-diode (LED) as the probe light source and a virtual lock-in camera as the detector [27]. Our system can measure the change in the OCT signal as a result of thermal expansion and refractive index change induced by MIR heating. First, we demonstrate 3D bond-selective imaging of 1 μm PMMA beads embedded in agarose gel, which confirms the isotropic 1-micron resolution of BS-FF-OCT. Second, we show 3D hyperspectral imaging of a polypropylene fiber mattress from a standard surgical mask and the comparison between BS-FF-OCT and FTIR to confirm the spectrum fidelity. Then, we demonstrate bond-selective volumetric imaging on biological samples, including cancer cell

Optics EXPRESS

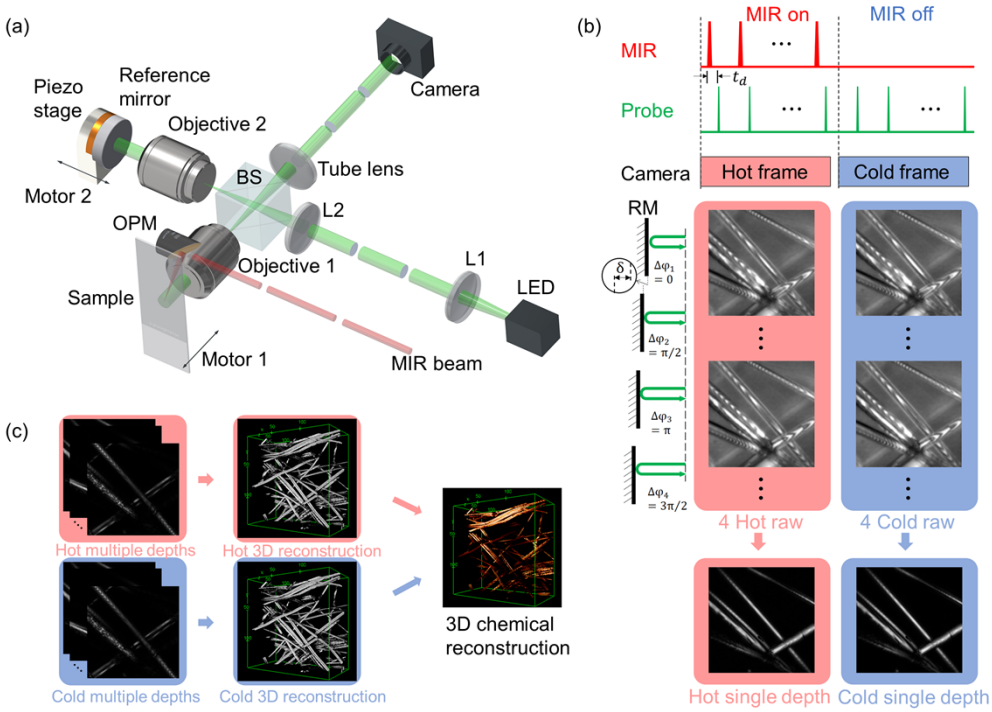

Fig. 1. BS-FF-OCT setup, synchronization, and image processing. (a) BS-FF-OCT setup configuration. BS: Beam-splitter. L1-2: Lens. LED: Light-emitting-diode. OPM: Off-axis parabolic mirror (90 degrees). (b) Synchronization and image acquisition at a single depth. RM: reference mirror. Camera captures "hot" and "cold" frames, where the MIR beam is respectively on and off in a sequence. MIR and probe pulses are synchronized, and the time delay (t_d) between them is optimized to detect the maximum photothermal signal. Reference mirror is shifted a certain distance (δ) 4 times to create 4 pairs (hot and cold) interference raw images, and then a pair of FF-OCT images at a specific depth is obtained by image processing. (c) Workflow of 3D image reconstruction. By combining FF-OCT images at multiple depths, 3D reconstruction images can be obtained. Finally, 3D bond-selective image can be obtained by subtracting the hot and cold 3D images. The sample in the demonstration figures is a polypropylene fiber mattress, which will be shown in more detail in Fig. 3.

spheroids and *C. elegans*. Finally, we demonstrate the capability of the BS-FF-OCT setup on imaging a highly scattering biological sample, i.e., myelinated axons in a mouse brain tissue slice, using an alternative pulse timing configuration.

2. Methods

2.1. BS-FF-OCT setup

A schematic of the BS-FF-OCT setup is shown in Fig. 1(a). The full-field optical coherence tomography (FF-OCT) is based on a Michelson interferometer. A broadband light-emitting diode (LED, UHP-T-545-SR, Prizmatix) provides Köhler illumination in both the sample and reference arms. Air objectives (SLMPLN50X, Olympus) are used in both arms. A CMOS camera (BFS-U3-17S7, FLIR) captures the wide-field interferometric image. The MIR beam comes from a mid-infrared optical parametric oscillator (Firefly-LW, M Squared Lasers), tunable from 1320 cm^{-1} to 1775cm^{-1}. The laser outputs a 20 kHz MIR pulse train. Then, the 20 kHz MIR pulse train is modulated at 50 Hz by an optical chopper system (MC2000B, Thorlabs). The

Optics EXPRESS

modulated MIR beam is focused by an off-axis parabolic mirror (MPD019-M03, Thorlabs) at the same side of the sample as the LED illuminates. The MIR pulse, LED probe pulse, optical chopper, and camera are synchronized by a pulse generator (9254-TZ50-US, Quantum composers) similar to the wide-field MIP microscopy [27]. The synchronized camera can capture exactly the corresponding images when the MIR beam is modulated on and off (corresponding "hot" and "cold" states of the sample). The details of the MIR and probe beam parameter, including the pulse widths, delays, powers, and illumination area are included in the support information Fig. S8 and Table. S1. The reference mirror is installed on a piezo stage (MIPOS 100 SG RMS, Piezosystem Jena) to shift the phase difference between the two arms. Both reference mirror (with the piezo stage) and sample are installed on motorized stages (Z825B, Thorlabs) to achieve automated and synchronized coherence and focal plane matching for volumetric image acquisition.

2.2. Automatic multi-depth scanning

The coherence plane shifting in FF-OCT is critical to match objective focal and coherence planes [7,59]. The coherence plane shift and its correction are shown in Fig. S6. When the system is imaging a specific depth of a sample, the coherence plane has to overlay with the focal plane (Fig. S6a). Then motor 1 scans the sample to the next depth. The coherence plane shifts and doesn't overlay with the new focal plane (Fig. S6b). Then, motor 2 has to scan a certain distance of the reference mirror to make the coherence plane overlay with the new focal plane (Fig. S6c). Software is developed to achieve automatic volumetric data acquisition in BS-FF-OCT. The software can automatically correct the coherence plane position by linearly shifting the reference mirror position at each depth during the multi-depth scanning, i.e., shifting $\Delta z/n$ at each depth in an (n + 1)-depths multi-depth acquisition, where Δz is the reference mirror shifting distance between the initial depth and the final depth. Manual correction is needed only at the initial depth and the final depth. The coherence plane can be corrected by linearly shifting the reference mirror position because the correction distance of the coherence plane has a linear relation with the sample shifting distance, as shown in the following equation [7],

$$\Delta z_{coherence\ plane} = \Delta z_{sample} \cdot \frac{n_{sample}^2 - n_{immersion}^2}{n_{sample} \cdot n_{immersion}} \tag{1}$$

where the n_{sample} is the refractive index of the sample, and $n_{immersion}$ is the refractive index of the immersion medium. $n_{immersion}$ is a constant and n_{sample} can be treated approximately as a constant for a common sample that usually does not contain large refractive index changes within the data acquisition depth range.

2.3. Theory and image reconstruction

The theory of the image reconstruction process at a specific depth of the sample is summarized below. At a specific depth (i.e., depth i) of the sample, 4 "cold" and 4 "hot" images are captured by the camera with 4 different phase shift values between the sample arm and the reference arm. The detected photothermal FF-OCT image from the sample's depth i, $I^i_{photothermal}$, is reconstructed using the equation below (detailed derivation is shown in the support information)

$$I^i_{photothermal} = \sqrt{(I_1^{cold} - I_3^{cold})^2 + (I_2^{cold} - I_4^{cold})^2} - \sqrt{(I_1^{hot} - I_3^{hot})^2 + (I_2^{hot} - I_4^{hot})^2} \tag{2}$$

The photothermal image at the sample's depth i reconstructed by Eqs. (2) can be further expressed as follows,

$$I^i_{photothermal} = \Delta E_{sample} + E^{cold}_{sample} \cdot [1 - \Gamma(\Delta OPL_{sample})] \tag{3}$$

Optics EXPRESS

where E^{cold}_{sample}, is the reflection field from the sample's depth i in the "cold" state of the sample. The ΔE_{sample} and $\Gamma(\Delta OPL_{sample})$ represent the photothermal-induced reflection field change and coherence change, respectively. The detailed definitions are shown in the support information.

Then a 1-D model of the sample is analyzed to further explain the origin of the detected photothermal signal by calculating ΔE_{sample}, E^{cold}_{sample} and ΔOPL_{sample} in Eq. (3). Assume there is a target layer at the depth i (the depth is z_i) of the sample, and the refractive index (for the probe wavelength) of the target layer is n_{target}. And assume the part above this target layer is a uniform medium with a refractive index (for the probe wavelength) of n_{medium} (assuming $n_{target} > n_{medium}$). And assume that the MIR absorption coefficient of the target layer is much larger than the medium (which is true since the medium is usually carefully chosen to avoid MIR absorption), thus the temperature change of the target layer, ΔT_{target}, is much larger than the medium, ΔT_{medium}. Assume the medium attenuation coefficients of the MIR beam and the probe beam are $\mu_{MIR\ att\ medium}$ and $\mu_{probe\ att\ medium}$, then the MIR intensity and the probe intensity at depth i can be written as, $I_{MIR}(z_i) = I_{MIR}(0) \cdot e^{-\mu_{MIR\ att\ medium} \cdot z_i}$, $I_{probe}(z_i) = I_{probe}(0) \cdot e^{-\mu_{probe\ att\ medium} \cdot z_i}$, respectively. Then the probe field at depth i can be written as $E_{probe}(z_i) = E_{probe}(0) \cdot e^{-\frac{1}{2}\mu_{probe\ att\ medium} \cdot z_i}$. Then the reflection field at depth i, E^{cold}_{sample} can be written as, (considering the attenuation of the returning trip, the $\frac{1}{2}$ factor disappears)

$$E^{cold}_{sample} = E_{probe}(0) \cdot e^{-\mu_{probe\ att\ medium} \cdot z_i} \cdot \frac{n_{target} - n_{medium}}{n_{target} + n_{medium}} \tag{4}$$

The optical path length can be written as,

$$OPL^{cold}_{sample} = 2 \cdot z_i \cdot n_{medium} \tag{5}$$

Differentiate Eq. (4) and (5) with temperature T, and considering $\Delta T_{target} \propto I_{MIR}(z_i)$, $\Delta T_{medium} \propto \int_0^{z_i} I_{MIR}(z)dz/z_i$ (average MIR intensity over the depth range of the medium), ΔE_{sample} and ΔOPL_{sample} can be approximated as,

$$\begin{aligned} \Delta E_{sample} &\approx E_{probe}(0) \cdot e^{-\frac{1}{2}\mu_{probe\ att\ medium} \cdot z_i} \cdot \frac{1}{(n_{target} + n_{medium})^2} \cdot \frac{\partial n_{target}}{\partial T} \cdot \Delta T_{target} \\ &\propto e^{-\frac{1}{2}\mu_{probe\ att\ medium} \cdot z_i} \cdot e^{-\mu_{MIR\ att\ medium} \cdot z_i} \end{aligned} \tag{6}$$

$$\begin{aligned} \Delta OPL_{sample} &\approx \left(\frac{\partial n_{medium}}{\partial T} + \frac{\partial l_{medium}}{l \cdot \partial T} \cdot n_{medium} \right) \cdot 2 \cdot z_i \cdot \Delta T_{medium} \\ &\propto (1 - e^{-\mu_{MIR\ att\ medium} \cdot z_i}) \end{aligned} \tag{7}$$

In which the $\frac{\partial n_{target}}{\partial T}$, $\frac{\partial n_{medium}}{\partial T}$, and $\frac{\partial l_{medium}}{l \cdot \partial T}$ are the thermo-optic and thermal-expansion coefficients of the target or the medium, respectively.

Equation (3) shows that the detected photothermal FF-OCT signal includes both the signal from ΔE_{sample} (change of the reflection of one specific target layer) and ΔOPL_{sample} (change of the optical path length of all the layers above the target layer). The interferograms of the coherence functions of the hot and cold states in Fig. S11 can also intuitively show that the measured photothermal signal is from both parts. Although the photothermal-induced change from the ΔE_{sample} is usually small (compared with E^{cold}_{sample}) due to the small thermo-optic coefficient ($\sim 10^{-4}$), the signal from the $E^{cold}_{sample} \cdot [1 - \Gamma(\Delta OPL_{sample})]$ can be much larger due to the ΔOPL_{sample} increasing with depth and can be comparable to E^{cold}_{sample} (when ΔOPL_{sample} is comparable to the coherence length). From Eqs. (6) and (7), we can see that ΔE_{sample} decreases when the detection depth increases due to the attenuation of both the MIR and the probe beam,

Optics EXPRESS

which usually induces a "shadow effect" for the deeper layers. ΔOPL_{sample} increases when the detection depth increases due to the accumulated depth range being heated by the MIR beam increase, which can decrease the "shadow effect".

2.4. FF-OCT sensitivity characterization

Accordingly to the equation in [60], the sensitivity of the FF-OCT setup is defined by the minimum detectable (when SNR = 1) coherent reflection of the sample (R_{min}),

$$R_{min} = 0.4 \cdot \frac{(R_{ref} + 2\,R_{inc})^2}{N\,\xi_{sat} R_{ref}} \tag{8}$$

in which, the R_{ref} is the reflection of the reference mirror (4% in our case), R_{inc} is the incoherent reflection from the sample, which is about 10% in our case, N is the number of total images acquired (average 100 images in our case), ξ_{sat} is the full well capacity of the camera (100 k in our case).

Substituting all of those values, R_{min} for our setup is about 5.8×10^{-8}. The actually measured coherent reflection of the samples, cell spheroids: 0.06%, *C. elegans*: 0.1%, and brain tissue: 0.4%, are all far beyond the theoretical sensitivity limit of our FF-OCT system.

2.5. Sample preparation

Polymethyl methacrylate (PMMA) beads embedded in agar gel sample preparation process is as follows. 1 mg agarose powder (Ultrapure Agarose, 16500-500) is measured and blended with 800 µL DI water and 200 µL 1 µm PMMA bead suspension (Phosphorex, MMA1000). Then the suspension is heated on a 95 °C hot plate until the agarose powder is melted. One 50 µm thick spacer is put on top of a CaF_2 substrate. Then the CaF_2 substrate with the space and a CaF2 coverslip are preheated to 95 °C to avoid instant solidification when the hot agar gel suspension contacts with the cold CaF_2 substrate or coverslip. The temperature of the sample suspension and the CaF_2 substrate has to be below 100 °C to avoid water boiling during sample preparation. 50 µL hot sample suspension is dropped on the CaF_2 substrate, and then the CaF_2 coverslip is put on top of the CaF_2 substrate to sandwich the sample suspension. Finally, the sample cools down at room temperature and solidifies.

The polypropylene fiber mattress sample is made by peeling off the melt-blown fabric layer from a regular surgical mask. Then the polypropylene fiber layer is fixed on a silicon substrate by double-sided tape.

The mouse brain tissue, *C. elegans*, and T24 human bladder cancer cell spheroids sample are prepared as follows. First, the fresh mouse brain (Charles River Labs Inc, BIOSPECIMEN - BRAIN - MOUSE) is fixed in 10% formalin and sliced into 150-µm-thick slices. The wild type *C. elegans* adults and T24 human bladder cancer cell spheroids are fixed in 10% formalin. Then the samples are washed in D_2O-based phosphate-buffered saline (PBS) buffer three times. Then, the washed samples are sandwiched between the CaF_2 substrate and the CaF_2 coverslip. Finally, the gap between the substrate and the coverslip is sealed with nail polish.

2.6. Images denoising

The BM4D denoising method is by an open-source demo software for BM4D volumetric data denoising (release ver. 3.2, 30 March 2015) [61]. The parameter values used are as follows. Noise standard deviation given as the percentage of the maximum intensity of the signal, 11%; noise distribution is Gaussian; BM4D parameter profile, modified profile; enable Wiener filtering; verbose mode; enable sigma estimation.

Optics EXPRESS

2.7. FTIR measurement

The FTIR spectrum is measured by a commercial FTIR spectroscopy (Nicolet FT-IR with ATR), which is a high-end optical benchtop system with 0.09 cm^{-1} resolution and continuous dynamic alignment. This unit allows AutoTune and automated continuously variable aperture adjustment. A horizontal attenuated total reflectance (HATR) accessory is also available.

2.8. Spectrum smoothing

The Gaussian-weighted moving average filter used in this work is realized by the "smoothdata" function in MATLAB R2021b. "Gaussian" window is chosen.

3. Results

3.1. BS-FF-OCT principles, instrumentation, and image reconstruction

BS-FF-OCT relies on the modulation of the OCT signal by the photothermal effect induced by the MIR beam. The setup shown in Fig. 1(a) is compartmentalized into two sub-systems: (1) FF-OCT and (2) MIR modulation. For the FF-OCT part, the light source is a broadband light-emitting-diode (LED, central wavelength: 545 nm, FWHM: 100 nm). The reference mirror (reflectivity: 4%) is placed on a piezo scanner to create phase shifting between the reference and sample arms. Both the sample and reference mirrors are installed on motorized stages to scan different depths of the sample. For the MIR modulation part, a tunable MIR laser from 1320 cm^{-1} to 1775cm^{-1} (linewidth: 10 cm^{-1}), covering the fingerprint region is used. The MIR and probe beams illuminate the sample from the same side.

The setup captures the depth-resolved photothermal FF-OCT images at a specific depth of the sample using a virtual lock-in technique [27], as shown in Fig. 1(b). The top panel of Fig. 1(b) shows the timing configuration of the probe, MIR pulses, and camera exposure. The MIR pulse has a 20 kHz repetition rate and is modulated to "on" and "off" duty cycles by an optical chopper at 50 Hz. The probe pulse repetition rate is also set to 20 kHz which is synchronized with the MIR pulse with a specific delay time to optimize the photothermal signal. The optimized delay time usually equals zero when the photothermal signal is majorly from the absorber itself rather than the surrounding medium. The camera frame rate is 100 Hz and is synchronized with the modulated "on" and "off" duty cycles of the MIR pulse. The camera-captured frames that correspond to the "on" and "off" duty cycles are called "hot" and "cold" frames, respectively. The middle panel of Fig. 1(b) shows that at each phase position of the reference mirror, a set of "hot" and "cold" raw frames are captured (to be averaged to 1 "hot" frame and 1 "cold" frame), and there are in total 4 phase positions. The bottom panel of Fig. 1(b) shows that 1 "hot" or "cold" FF-OCT image is obtained from the 4 "hot" or "cold" averaged raw frames, using the 4-frame phase-shifting algorithm [7] (as the detailed derivations shown in the support information). Then, the depth-resolved photothermal FF-OCT image at this specific depth can be obtained by subtracting the "hot" and "cold" FF-OCT images. (as shown in Eq. (13) in the method section) Furthermore, to obtain 3D reconstructed images for both hot and cold states, as shown in Fig. 1(c), the sample is scanned at different depths with automatic coherence plane correction within the imaging volume (see details in the methods section). A 3D bond-selective OCT map can be obtained by subtracting the hot and cold 3D reconstructed images.

3.2. BS-FF-OCT system characterization

To characterize the BS-FF-OCT setup, we first demonstrate 3D bond-selective imaging of 1 μm Poly(methyl methacrylate) (PMMA) beads embedded in agarose gel. Figure 2 shows that BS-FF-OCT achieves label-free volumetric vibrational spectroscopic imaging at isotropic 1-micron resolution. Specifically, Fig. 2(a-c) shows the cold FF-OCT, on-resonance, and off-resonance BS-FF-OCT images captured at three different depths with 0.5 μm step size. First,

Optics EXPRESS

the cold FF-OCT images in Fig. 2(a) distinguish beads suspended at different depths (i.e., 1 μm apart), showing the depth-resolving capability of BS-FF-OCT setup. Second, to demonstrate the bond-selective capability, the MIR beam is set to an on-resonance absorption peak of PMMA at 1730cm^{-1}. The BS-FF-OCT images show consistent features as in cold FF-OCT images (see Fig. 2(a-b)). Yet, the off-resonance BS-FF-OCT images at 1770cm^{-1} show weak contrast of beads, as shown in Fig. 2(c). Figure 2(d-e) are the zoom-in views of a selected imaging 3D volume from three different directions. Figures 2(d)$_1$ and ;2(e)$_1$ are the corresponding areas indicated by the dashed squares in Figs. 2(a)$_\mathbf{2}$ and 2(b)$_\mathbf{2}$, respectively. It can be seen from Fig. 2(d-e) that the beads have a slightly longer dimension along the optical axis. To characterize the axial and lateral resolution quantitatively, the 1D line profiles across the selected bead are plotted in Fig. 2(f). The full-width half maximum (FWHM) of these line profiles are as follows, 942.5 nm (green in (f$_1$)), 824.4 nm (black in (f$_1$)), 787.3 nm (blue in (f$_2$)), 772.7 nm (black in (f$_2$)), 870.3 nm (purple in (f$_3$)) and 1156.7 nm (black in (f$_3$)). This result demonstrates the isotropic 1-μm resolution of the BS-FF-OCT setup. As a pump-probe technique, the resolution of the BS-FF-OCT setup is determined by the wavelength and optics of the probe beam [19]. For FF-OCT, the axial resolution (Δz) [7] can be calculated as $\Delta z = \left(\frac{1}{\Delta z_s{}^2} + \frac{1}{\Delta z_{NA}{}^2}\right)^{-\frac{1}{2}}$, where $\Delta z_s = \frac{2\ln(2)}{n\cdot\pi}\cdot\frac{\lambda_0^2}{\Delta\lambda}$, which corresponding the coherence length, and $\Delta z_{NA} = \frac{n\cdot\lambda_0}{NA^2}$, which corresponding to the focal depth. The lateral resolution (Δr) can be calculated as $\Delta r = \frac{\lambda_0}{2\cdot NA}$. Substituting $\lambda_0 = 545\ nm$, $\Delta\lambda = 100\ nm$, $n = 1.33$, $NA = 0.35$, the theoretical axial resolution Δz can be calculated to be 972.1 nm, $\Delta z_s = 985.5\ nm$, $\Delta z_{NA} = 5917\ nm$, and the theoretical lateral resolution Δr can be calculated to be 778.6 nm. Since $\Delta z_{NA} \gg \Delta z_s \approx \Delta z$, we can see that the coherence length is the limiting factor of the axial resolution. The theoretical axial and lateral resolution values are roughly consistent with the experimental FWHM values shown in Fig. 2(f).

It is noteworthy that there are also some PMMA particles within the MIR illumination area that don't show contrast in the photothermal image, which is due to the maximum contrast of the cold image and the photothermal image may not be at the same depth (as shown in Fig. S12). We can see that, the PMMA bead only showing contrast in the cold frame (indicated by the red arrow in Fig. S12) shows the maximum cold and photothermal contrast at different depths. And all the PMMA particles within the MIR illumination area show photothermal contrast in the sum image of different depths (Fig. S12d).

3.3. BS-FF-OCT imaging of polypropylene fiber mattress

To demonstrate the 3D spectroscopic imaging capability of BS-FF-OCT, we use polypropylene fiber mattress from a standard surgical mask in air as a testbed (Fig. 3). To emphasize the depth-resolving capability of BS-FF-OCT, which is the primary novelty compared to the conventional wide-field MIP [27], the wide-field cold, on-resonance, and off-resonance MIP images at different depths are captured as shown in Fig. 3(a-c). Those wide-field images are captured at different focus positions, and they are obtained under the same experimental condition and acquisition parameters, except that the reference arm is blocked, which makes a fair comparison to those of BS-FF-OCT. As shown in Fig. 3(a-c), the depth-resolving capability of conventional wide-field MIP [27] imaging is very limited, where the fiber features are indistinguishable. In contrast, BS-FF-OCT images in Fig. 3(d-f) clearly resolve features at different depths. Both wide-field MIP images and BS-FF-OCT images demonstrate bond-selective capability, i.e., at the C-H asymmetric deformation vibration bond at around 1450 cm^{-1}. While Figs. 3(b) and 3(e) both show bright contrast, no contrast was found at the 1600 cm^{-1} off-resonance wavenumber images (see Figs. 3(c) and 3(f)). To further show the 3D imaging capability of BS-FF-OCT, we perform 3D reconstruction of the polypropylene fiber mattress for a total depth range of 75 μm (see Fig. 3(g)). We notice that each fiber strip in Fig. 3(g) shows "double strips" which can be seen more clearly in the Visualization 1, Visualization 2, Visualization 3. Since FF-OCT measures back reflections

Optics EXPRESS

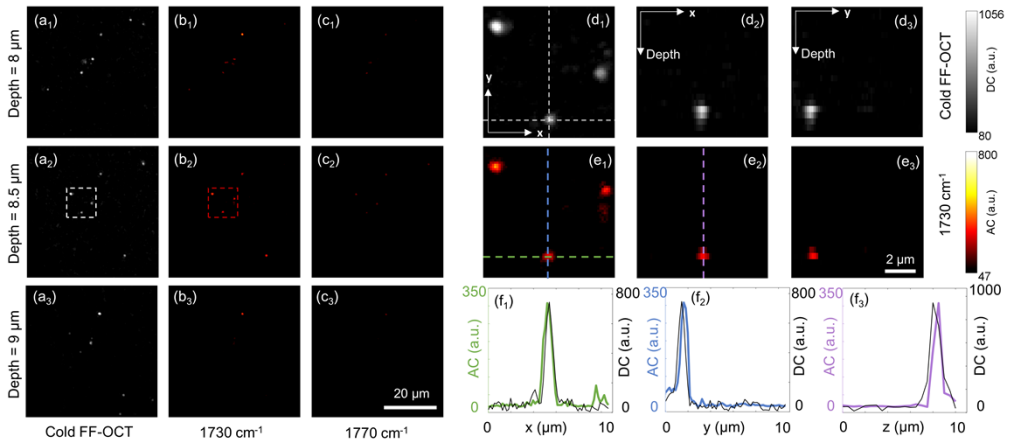

Fig. 2. BS-FF-OCT imaging of 1 μm PMMA beads embedded in agarose gel. (a) cold FF-OCT images at different depths. (b-c) BS-FF-OCT images at 1730cm^{-1} and 1770cm^{-1}. 1730cm^{-1} is the C = O band in PMMA, and 1770cm^{-1} is at off-resonance**. (d_1) zoom-in view of the white dashed square area in (a_2). (d_{2-3}) cross-sectional images along the dashed lines in (d_1). (e_{1-3}) corresponding BS-FF-OCT images at 1730cm^{-1} of (d_{1-3}). (f_{1-3}) 1D cross-line profiles corresponding to the colored dashed lines in (e_{1-2}).** The black profiles correspond to the cold FF-OCT images. FWHM of line profiles: 942.5 nm (green in (f_1)), 824.4 nm (black in (f_1)), 787.3 nm (blue in (f_2)), 772.7 nm (black in (f_2)), 870.3 nm (purple in (f_3)) and 1156.7 nm (black in (f_3)). BS-FF-OCT images are normalized by MIR powers. All intensity values are in linear scales. Image sizes: (a-c) 50 μm (280 pixels) × 50 μm (280 pixels), (d_1, e_1) 10 μm (56 pixels) × 10 μm (56 pixels), (d_{2-3}, e_{2-3}) 10 μm (56 pixels) × 10 μm (20 depths).

from the sample, the air-polypropylene top and polypropylene-air bottom interfaces of each fiber strip create two distinguishable strips. Also, the diameter of each fiber strip is larger than the axial resolution of the setup thus we can see the two reflection interfaces. Fig. 3(h) shows the BS-FF-OCT spectrum extracted from the position indicated by the green arrow in Fig. 3(e)$_2$ and comparison with the FTIR spectrum. Both BS-FF-OCT and FTIR spectra show peaks for the C-H symmetric deformation vibration bond at around 1370 cm^{-1} and the C-H asymmetric deformation vibration bond at around 1450 cm^{-1}. These results further verify the bond-selective capability and demonstrate good spectral fidelity.

3.4. *BS-FF-OCT imaging of human bladder cancer cell spheroids and C. elegans*

It has been demonstrated that mid-infrared photothermal microscopes are useful tools for biomedical study and disease diagnosis, e.g., imaging the lipid distribution in living cells for cancer diagnosis and imaging the protein secondary structure for Alzheimer's disease diagnosis [40]. As a new technique in the mid-infrared photothermal microscope family, the proposed BS-FF-OCT also has great potential in biomedical imaging applications. Furthermore, compared to other mid-infrared photothermal microscope modalities, BS-FF-OCT has a unique advantage in imaging highly scattering 3D biological samples, benefiting from the implementation of FF-OCT.

To demonstrate the broad application potential of BS-FF-OCT on biological samples, we first use human bladder cancer cell spheroids and *C. elegans* as testbeds. Figure 4 shows the BS-FF-OCT images of human bladder cell spheroids. The high-density areas (cytoplasm) and low-density areas (nucleus, two examples are indicated by the red dashed line areas in Fig. 4(b)$_2$) inside the cell spheroids volume can be seen clearly (see Fig. 4(b)). Features from different

Optics EXPRESS

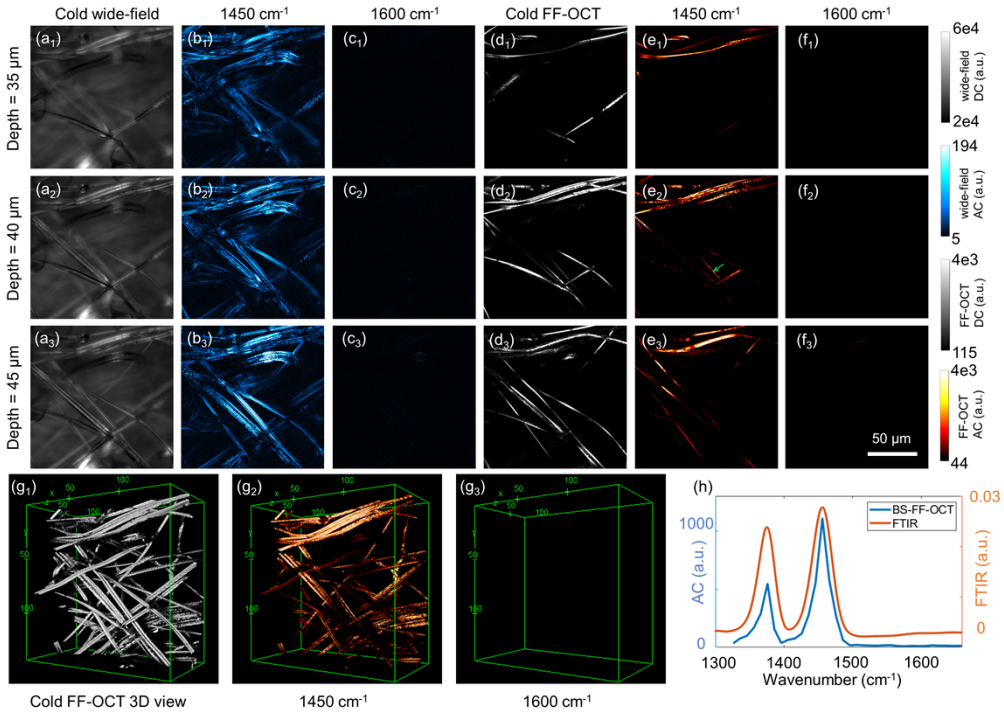

Fig. 3. BS-FF-OCT imaging of polypropylene fiber mattress. (a) cold wide-field images at different depths. **(b-c) wide-field MIP images at 1450 cm^{-1} and 1600 cm^{-1}.** 1450 cm^{-1} is the C-H asymmetric deformation vibration bond in polypropylene, and 1600 cm^{-1} is at off-resonance**. (d) cold FF-OCT images at different depths**. **(e-f) BS-FF-OCT images at 1450 cm^{-1} and 1600 cm^{-1}. (g) 3D reconstruction of cold FF-OCT and BS-FF-OCT images.** (from a view direction that slightly offsets the direction facing the XY plane) **(h) comparison of BS-FF-OCT and FTIR spectrum.** The BS-FF-OCT spectrum is extracted from the position in (e_2) indicated by the green arrow. FTIR spectrum is acquired by a commercial FTIR spectroscopy from a bulky measurement of the polypropylene fiber sample. BS-FF-OCT images and spectrum are normalized by MIR powers. All images are denoised by BM4D algorithm. BS-FF-OCT and FTIR spectrum is smoothed by Gaussian-weighted moving average filter. All intensity values are in linear scales. Image sizes: (a-f) 144 μm (800 pixels) × 144 μm (800 pixels), (g) 144 μm (800 pixels) × 144 μm (800 pixels) × 75 μm (75 depths).

depths can be distinguished compared to the cold wide-field images in Fig. 4(a). Figures 4(c), and 4(d) confirm the bond-selective capability, i.e., at 1650 cm^{-1} (see Fig. 4(c)) in resonance with the amide I band of proteins where there is a stronger photothermal contrast than that of at off-resonance 1775cm^{-1}(see Fig. 4(d)). Moreover, the cutting-through sectioning images along the axial direction of the dashed lines in Fig. 4(c)$_2$ show the cytoplasm and nucleus areas from the side views (see Fig. 4(e)).

Figure 5 shows the BS-FF-OCT images of *C. elegans*. The cold FF-OCT images in Fig. 5(b) show features inside the *C. elegans* worm at various depths. In contrast, scatterers from different planes hinder these futures in the cold wide-field images due to the lack of optical-sectioning capability (see Fig. 5(a)). The BS-FF-OCT images in Fig. 5(c) show strong photothermal contrast at 1650 cm^{-1}, amide I band whereas the photothermal contrast at the 1770cm^{-1} off-resonance wavenumber in Fig. 5(d) is weak. This confirms the chemical selective capability since the *C. elegans* is rich in protein. To further demonstrate the 3D sectioning capability of the BS-FF-OCT

Optics EXPRESS

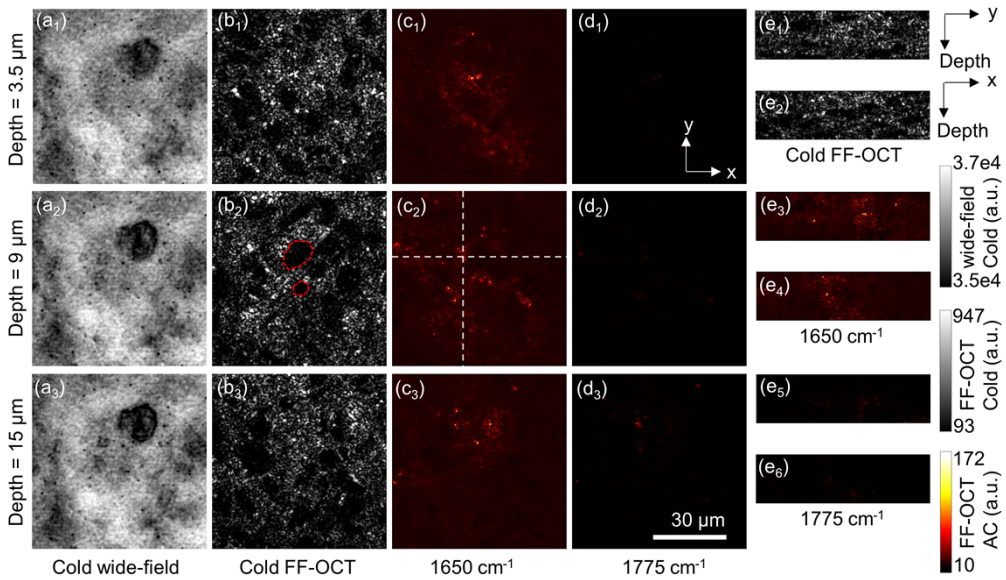

Fig. 4. BS-FF-OCT imaging of cancer cell spheroids. (a) Cold wide-field images at different depths. (b) cold FF-OCT images at different depths. (c-d) BS-FF-OCT images at 1650 cm^{-1}, and 1775cm^{-1}. 1650 cm^{-1} is the amide I band in protein, and 1775cm^{-1} is at off-resonance**. (e) Cross-sectional images along the dashed lines in (c_2).** BS-FF-OCT images are normalized by MIR powers. All intensity values are in linear scales. Image sizes: (a-d) 72 µm (400 pixels) × 72 µm (400 pixels), (e) 72 µm (400 pixels) × 20 µm (40 depths).

setup, the cutting-through sectioning images along the axial direction and dashed lines shown in Fig. 5$(b)_1$-$(d)_1$ are plotted in Fig. 5(e-g). In these side views, the different structures inside the worm are shown more clearly.

3.5. *BS-FF-OCT imaging of myelinated axons in mouse brain tissue*

We choose a region containing myelinated axons in a mouse brain tissue slice (Fig. 6) as the testbed to demonstrate the application potential of our setup for imaging highly scattering biological samples. Martin Schnell *et al.* previously demonstrated infrared spectroscopic imaging of biological tissues through a Mirau interference objective, where the tissue sample is only 5 µm thick. [31] In this work, we demonstrate BS-FF-OCT imaging up to 20 µm depth of the myelinated axons region in a mouse brain tissue. The BS-FF-OCT setup can image thicker tissues owing to its particular design. The reference arm is fixed in the study by Martin Schnell *et al.* [31], since a Mirau objective is adopted to generate the interference signal. In contrast, BS-FF-OCT is based on a time-domain FF-OCT with a separated and tunable reference arm. Thus, in our BS-FF-OCT setup, the coherence plane can be tuned to the deeper layers of the samples, as long as there are enough backscattering photons. Fig. 6(a) shows the cold wide-field reflection images focused at different depths. Due to limited depth-resolving capability, Fig. 6(a) looks similar at all depths. The photothermal wide-field reflection images focused at different depths shown in Fig. S1 also look similar. In comparison, the cold FF-OCT brain tissue images can distinguish myelinated axon structures from different depths (see Fig. 6(b)).

Second, an alternative MIR and probe pulse timing configuration is adopted to maximize the detected photothermal signal. Simulations by Zong *et al.* demonstrate that photothermal cooling time increases with the sample size [36] (a similar simulation result is also shown in the support

Optics EXPRESS

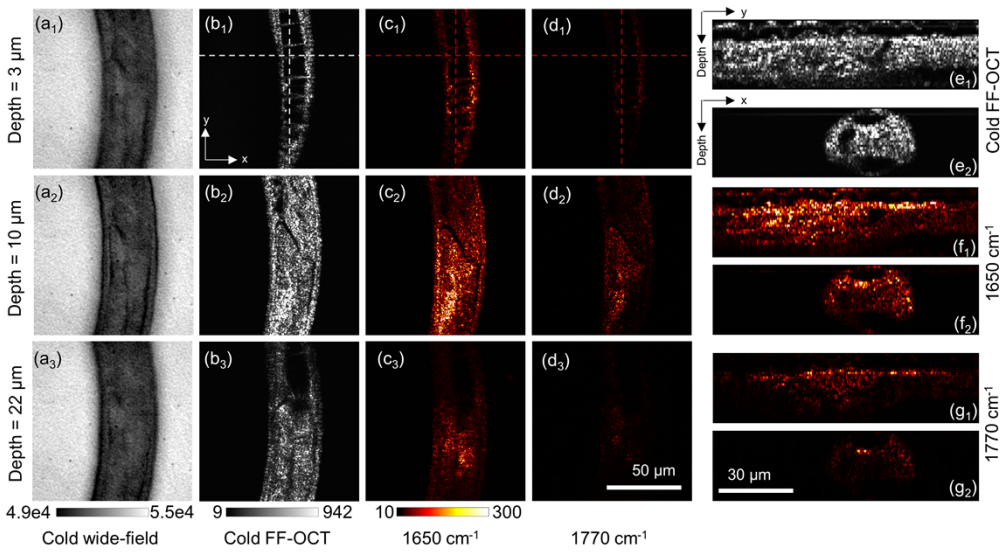

Fig. 5. BS-FF-OCT imaging of *C. elegans*. (a) cold wide-field images at different depths. **(b) cold FF-OCT images at different depths**. **(c-d) BS-FF-OCT images at 1650 cm^{-1}, and 1770cm^{-1}.** 1650 cm^{-1} is the amide I band in protein, and 1770cm^{-1} is at off-resonance**. (e-g) cross-sectional images along the dashed lines in (b_1), (c_1), and (d_1).** BS-FF-OCT images are normalized by MIR powers. All intensity values are in linear scales. Image sizes: (a-d) 108 µm (600 pixels) × 108 µm (600 pixels), (e-g) 108 µm (600 pixels) × 28 µm (28 depths). The unit of all the color calibration bars is the arbitrary unit (a.u.).

information Fig. S9). A suitable heating and probe pulse width and timing configuration is important in photothermal measurement to achieve either thermal confinement [44] or improve the photothermal signal [55]. Because this study covers the samples with very different sizes (the smallest, 1 µm PMMA beads, and the very bulky sample, brain tissue with a total thickness of 150 µm), different pulse widths and timing configurations are needed for different samples. (details are shown in the support information Table. S1) The maximum photothermal signal can be obtained when the temperature difference between the "hot" and "cold" states is largest. Therefore, there should be enough time between the probe pulses to differentiate the "hot" and "cold" states. In the pulse timing configuration shown in Fig. 1(b), the time window between the first probe pulse for the "cold" state and the last probe pulse for the "hot" state is only 50 µs, which is not enough for the cooling of the 150-µm-thick brain tissue. Thus, a new timing configuration is added to the setup, as shown in Fig. S3. The maximum cooling time in this alternative timing configuration is limited to 9 ms by the camera period time (10 ms) and the MIR pulse train width (1 ms). MIR-probe delay scan is also performed, as shown in Fig. S4 and Fig. S5. The cooling time constant of the 150-µm-thick brain tissue is found to be about 1.21 ms, showing that this thick tissue sample indeed requires an alternative timing configuration. Using the optimized MIR-probe delay value (0 ms) shown in Fig. S5a, BS-FF-OCT imaging results of myelinated axons of different depths are shown in Fig. 6(c-e). At the 1650 cm^{-1} Amide I and 1740cm^{-1} C = O bands, the BS-FF-OCT contrast is strong whereas the images at the 1775cm^{-1} off-resonance wavenumber have very weak contrast. This result reflects the major chemical content of myelinated axons, i.e., protein and lipids. The 3D reconstruction results of the cold FF-OCT and BS-FF-OCT images at 1650 cm^{-1} and 1775cm^{-1} are shown in Fig. 6(f).

To demonstrate the chemical selectivity, hyperspectral BS-FF-OCT imaging was performed. Fig. 6(g) shows the BS-FF-OCT spectrum extracted from another dataset shown in support

Optics EXPRESS

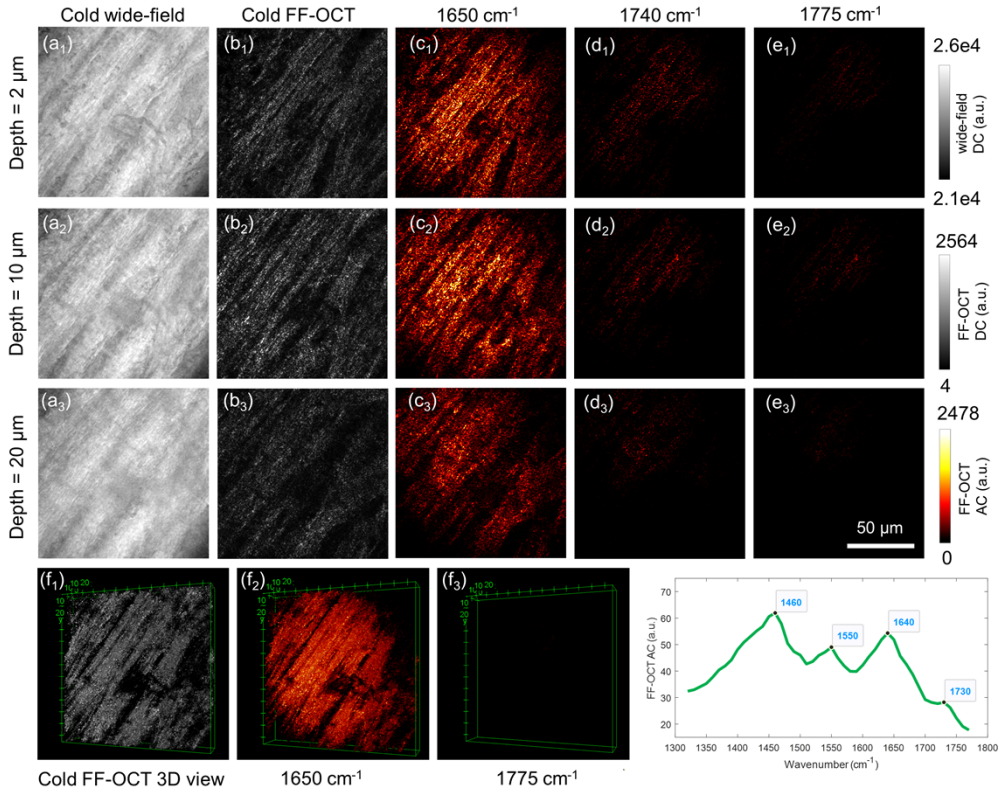

Fig. 6. BS-FF-OCT imaging of myelinated axons in mouse brain tissue. (a) cold wide-field images at different depths. (b) cold FF-OCT images at different depths. (c-e) BS-FF-OCT images at 1650 cm^{-1}, 1740cm^{-1}, and 1775cm^{-1}. 1650 cm^{-1} is the amide I band in protein, 1740cm^{-1} is the C = O band in lipids, and 1775cm^{-1} is at off-resonance**. (f) 3D reconstruction of cold FF-OCT and BS-FF-OCT images.** (from a view direction that slightly offsets the direction facing the XY plane) **(g) BS-FF-OCT spectrum.** The BS-FF-OCT spectrum is extracted from another dataset shown in the support information Fig. S10. BS-FF-OCT Images and spectrum are normalized by MIR powers. All images are denoised by BM4D algorithm. BS-FF-OCT spectrum is smoothed by Gaussian-weighted moving average filter. All intensity values are in linear scales. Image sizes: (a-e) 144 μm (800 pixels) × 144 μm (800 pixels), (f) 144 μm (800 pixels) × 144 μm (800 pixels) × 20 μm (40 depths).

information Fig. S10. The spectrum shown in Fig. 6(g) is smoothed to reduce the noise level. The raw spectrum is shown in the supporting information Fig. S2. The peak positions (1550 cm^{-1}, 1640 cm^{-1}, 1730cm^{-1}) shown in the spectrum are consistent with the peak positions for amide II (1550 cm^{-1}), amide I (1650 cm^{-1}), and the C = O band (1740cm^{-1}) in protein and lipids, respectively. The other peak shown at 1460 cm^{-1} is altered from the amide II band with the deuterium-oxide-based environment [62] (i.e., the water-based environment is not used due to the MIR absorption of water). The spectrum is consistent with the result in the literature [63] except for the peak at 1460 cm^{-1}.

4. Discussion and limitations

We present a 3D chemical imaging technology termed bond-selective full-field optical coherence tomography (BS-FF-OCT). The capability of BS-FF-OCT is demonstrated on polymer samples,

Optics EXPRESS

including 1-micron PMMA beads and polypropylene fibers, and biological samples, including mouse brain tissue, *C. elegans*, and human bladder cancer cell spheroids. Our BS-FF-OCT setup has demonstrated the ability to image up to 20 µm depth of highly scattering biological tissue. It is noteworthy that the main factor that limits the imaging depth is the strong tissue scattering of the visible probe beam, rather than the absorption of the mid-infrared beam. The absorption length of the mid-infrared beam depends on the wavenumber and the sample. For example, the mid-infrared penetration depth on skin tissue can reach 50 ~ 100 µm [64], depending on the water content. Since we are using deuterium oxide as the medium to avoid the absorption of the water at 1500 cm^{-1} ~ 1750cm^{-1}, the mid-infrared penetration depth could reach at least 100 µm.

Furthermore, our setup is capable of imaging highly scattering samples, which is beyond the reach of phase tomography. With BS-FF-OCT, the high-density areas (cytoplasm) and the low-density areas (nucleus) inside a cell spheroid can be resolved. Compared to other imaging methods, such as MUSE [65] and SRS [15], the demonstrated BS-FF-OCT has clear advantages. BS-FF-OCT is a label-free method, while the MUSE requires fluorescent dye labeling, and it only detects the surface by UV excited fluorescence. Compared to SRS, our mid-infrared photothermal approach benefits from a much larger mid-infrared absorption cross-section of vibrational bonds compared to that of Raman scattering, as reviewed in [39]. Also, IR absorption is especially sensitive to fingerprint vibrations, such as the amide I band as a signature of protein secondary structure, while SRS is highly sensitive to high-wavenumber CH vibration. As a result, for myelin sheath, the SRS or CARS signal would predominantly arise from the lipid membrane that is rich in CH bonds. Instead, the photothermal OCT contrast arises from the proteins inside the myelin membrane. This complimentary relationship between Raman and IR opens a lot of opportunities for the reported BS-FF-OCT work. For example, we can potentially use this method to detect the protein secondary structure in brain slices, in which beta-sheet protein aggregate is a signature of neurodegenerative diseases.

Additionally, the full-field mode, which is key to high throughput analysis, is not possible with SRS microscopy or the scanning scheme of MIP. Compared to the previous scanning MIP [19], the imaging depth on biology samples of this work is similar. The advantage of this work is that it is not only a 3D IR imaging method but also a wide-field IR imaging method. And the wide-field (full-field) mode is the key to high throughput analysis. The 29 µm depth of view imaging of the cell (only one single cell) in [19] contains only 80*120*29 ≈ 0.28 mega voxels, and considering the 1 ms dwell time at each voxel, the acquisition costs about 5 min. While in this work, for example, the result of the brain tissue contains 800*800*40 ≈ 26 mega voxels, and considering the 8 s acquisition time at each depth, the total acquisition time is also about 5 min. The imaging speed (voxel number/time) is improved by 90 times due to the use of wide-field configuration.

Because this is the first concept demonstration study, there are still some limitations of the proposed method. First, all the tested biological samples are fixed. Living biological sample imaging has not been demonstrated yet. Second, the image reconstruction is performed after the raw image acquisition. Real-time BS-FF-OCT image reconstruction has not been achieved. Those limitations could be improved in future developments.

5. Conclusion

In summary, we demonstrate a bond-selective full-field OCT technique that enables label-free high throughput volumetric spectroscopic imaging at isotropic 1.0-micron resolution, with broad potential applications in biological imaging.

Funding. National Institutes of Health (R33CA261726, R35GM136223).

Disclosures. JXC discloses financial interest with Photothermal Spectroscopy Corp which did not support this work.

Data availability. Data underlying the results presented in this paper are not publicly available at this time but may be obtained from the authors upon reasonable request.

Optics EXPRESS

Author contributions

C.Y., M.S.Ü., and J.X.C. proposed the idea of BS-FF-OCT. M.S.Ü. and J.X.C. supervised the research team. J.X.C. and M.S.Ü. revised the final version of the manuscript. C.Y. designed and built the visible probing part of the experiment setup, wrote the single-depth cold FF-OCT image acquisition function of the data acquisition software, and performed initial cold FF-OCT imaging experiments. H.Z. designed and built the MIR part of the experiment setup, wrote the photothermal image acquisition, multi-depth scanning, and hyperspectral scanning functions of the data acquisition software, and performed BS-FF-OCT imaging experiment on polypropylene fiber. H.Z. and J.Z. optimized the MIR beam optical path and performed BS-FF-OCT imaging experiments on 1 μm PMMA beads, cell spheroids, and C. elegans. H.Z. processed the data, plotted figures, and wrote the first version of the manuscript. F.K.C. cultured the cell spheroids used in this manuscript. Z.A.W. cultured the C. elegans used in this manuscript. All authors contributed to the final creation of the manuscript.

Supplemental document. See Supplement 1 for supporting content.

References

1. W. Drexler and James G. Fujimoto, "Fujimoto," *Optical coherence tomography: technology and applications* (Springer, 2015), Vol. 2.
2. D. Huang, E. A. Swanson, C. P. Lin, J. S. Schuman, W. G. Stinson, W. Chang, M. R. Hee, T. Flotte, K. Gregory, C. A. Puliafito, and J. G. Fujimoto, "Optical Coherence Tomography," Science **254**(5035), 1178–1181 (1991).
3. A. F. Fercher, C. K. Hitzenberger, G. Kamp, and S. Y. El-Zaiat, "Measurement of intraocular distances by backscattering spectral interferometry," Opt. Commun. **117**(1-2), 43–48 (1995).
4. M. Wojtkowski, R. Leitgeb, A. Kowalczyk, T. Bajraszewski, and A. F. Fercher, "In vivo human retinal imaging by Fourier domain optical coherence tomography," J. Biomed. Opt. **7**(3), 457–463 (2002).
5. N. Nassif, B. Cense, B. H. Park, S. H. Yun, T. C. Chen, B. E. Bouma, G. J. Tearney, and J. F. de Boer, "In vivo human retinal imaging by ultrahigh-speed spectral domain optical coherence tomography," Opt. Lett. **29**(5), 480–482 (2004).
6. E. Beaurepaire, A. C. Boccara, M. Lebec, L. Blanchot, and H. Saint-Jalmes, "Full-field optical coherence microscopy," Opt. Lett. **23**(4), 244–246 (1998).
7. A. Dubois, *Handbook of full-field optical coherence microscopy: Technology and applications* (CRC Press, 2016).
8. V. Mazlin, P. Xiao, E. Dalimier, K. Grieve, K. Irsch, J.-A. Sahel, M. Fink, and A. C. Boccara, "In vivo high resolution human corneal imaging using full-field optical coherence tomography," Biomed. Opt. Express **9**(2), 557–568 (2018).
9. P. Mecê, J. Scholler, K. Groux, and C. Boccara, "High-resolution in-vivo human retinal imaging using full-field OCT with optical stabilization of axial motion," Biomed. Opt. Express **11**(1), 492–504 (2020).
10. J. R. Durkin, J. L. Fine, H. Sam, M. Pugliano-Mauro, and J. Ho, "Imaging of Mohs micrographic surgery sections using full-field optical coherence tomography: a pilot study," Dermatol. Surg. **40**(3), 266–274 (2014).
11. O. Assayag, M. Antoine, B. Sigal-Zafrani, M. Riben, F. Harms, A. Burcheri, K. Grieve, E. Dalimier, B. Le Conte de Poly, and C. Boccara, "Large field, high resolution full-field optical coherence tomography: a pre-clinical study of human breast tissue and cancer assessment," Technology in cancer research & treatment **13**, 455–468 (2013).
12. M. Jain, N. Shukla, M. Manzoor, S. Nadolny, and S. Mukherjee, "Modified full-field optical coherence tomography: A novel tool for rapid histology of tissues," Journal of pathology informatics **2**(1), 28 (2011).
13. J.-X. Cheng and X. S. Xie, "Vibrational spectroscopic imaging of living systems: An emerging platform for biology and medicine," Science **350**(6264), aaa8870 (2015).
14. G. Turrell and J. Corset, *Raman microscopy: developments and applications* (Academic Press, 1996).
15. C. W. Freudiger, W. Min, B. G. Saar, S. Lu, G. R. Holtom, C. He, J. C. Tsai, J. X. Kang, and X. S. Xie, "Label-free biomedical imaging with high sensitivity by stimulated Raman scattering microscopy," Science **322**(5909), 1857–1861 (2008).
16. F. Hu, L. Shi, and W. Min, "Biological imaging of chemical bonds by stimulated Raman scattering microscopy," Nat. Methods **16**(9), 830–842 (2019).
17. I. W. Levin and R. Bhargava, "Fourier transform infrared vibrational spectroscopic imaging: integrating microscopy and molecular recognition," Annu. Rev. Phys. Chem. **56**(1), 429–474 (2005).
18. M. J. Baker, J. Trevisan, P. Bassan, R. Bhargava, H. J. Butler, K. M. Dorling, P. R. Fielden, S. W. Fogarty, N. J. Fullwood, and K. A. Heys, "Using Fourier transform IR spectroscopy to analyze biological materials," Nat. Protoc. **9**(8), 1771–1791 (2014).
19. D. Zhang, C. Li, C. Zhang, M. N. Slipchenko, G. Eakins, and J.-X. Cheng, "Depth-resolved mid-infrared photothermal imaging of living cells and organisms with submicrometer spatial resolution," Sci. Adv. **2**(9), e1600521 (2016).
20. Z. Li, K. Aleshire, M. Kuno, and G. V. Hartland, "Super-Resolution Far-Field Infrared Imaging by Photothermal Heterodyne Imaging," J. Phys. Chem. B **121**(37), 8838–8846 (2017).
21. C. Li, D. Zhang, M. N. Slipchenko, and J.-X. Cheng, "Mid-Infrared Photothermal Imaging of Active Pharmaceutical Ingredients at Submicrometer Spatial Resolution," Anal. Chem. **89**(9), 4863–4867 (2017).
22. X. Li, D. Zhang, Y. Bai, W. Wang, J. Liang, and J.-X. Cheng, "Fingerprinting a Living Cell by Raman Integrated Mid-Infrared Photothermal Microscopy," Anal. Chem. **91**(16), 10750–10756 (2019).
23. P. D. Samolis and M. Y. Sander, "Phase-sensitive lock-in detection for high-contrast mid-infrared photothermal imaging with sub-diffraction limited resolution," Opt. Express **27**(3), 2643–2655 (2019).
24. I. M. Pavlovetc, K. Aleshire, G. V. Hartland, and M. Kuno, "Approaches to mid-infrared, super-resolution imaging and spectroscopy," Phys. Chem. Chem. Phys. **22**(8), 4313–4325 (2020).

Optics EXPRESS

25. J. Yin, L. Lan, Y. Zhang, H. Ni, Y. Tan, M. Zhang, Y. Bai, and J.-X. Cheng, "Nanosecond-resolution photothermal dynamic imaging via MHZ digitization and match filtering," Nat. Commun. **12**(1), 7097 (2021).
26. Y. Zhang, C. Yurdakul, A. J. Devaux, L. Wang, X. G. Xu, J. H. Connor, M. S. Ünlü, and J.-X. Cheng, "Vibrational Spectroscopic Detection of a Single Virus by Mid-Infrared Photothermal Microscopy," Anal. Chem. **93**(8), 4100–4107 (2021).
27. Y. Bai, D. Zhang, L. Lan, Y. Huang, K. Maize, A. Shakouri, and J.-X. Cheng, "Ultrafast chemical imaging by widefield photothermal sensing of infrared absorption," Sci. Adv. **5**(7), eaav7127 (2019).
28. M. Tamamitsu, K. Toda, R. Horisaki, and T. Ideguchi, "Quantitative phase imaging with molecular vibrational sensitivity," Opt. Lett. **44**(15), 3729–3732 (2019).
29. K. Toda, M. Tamamitsu, Y. Nagashima, R. Horisaki, and T. Ideguchi, "Molecular contrast on phase-contrast microscope," Sci. Rep. **9**(1), 9957 (2019).
30. D. Zhang, L. Lan, Y. Bai, H. Majeed, M. E. Kandel, G. Popescu, and J.-X. Cheng, "Bond-selective transient phase imaging via sensing of the infrared photothermal effect," Light: Sci. Appl. **8**(1), 116 (2019).
31. M. Schnell, S. Mittal, K. Falahkheirkhah, A. Mittal, K. Yeh, S. Kenkel, A. Kajdacsy-Balla, P. S. Carney, and R. Bhargava, "All-digital histopathology by infrared-optical hybrid microscopy," Proc. Natl. Acad. Sci. U. S. A. **117**(7), 3388–3396 (2020).
32. M. Tamamitsu, K. Toda, H. Shimada, T. Honda, M. Takarada, K. Okabe, Y. Nagashima, R. Horisaki, and T. Ideguchi, "Label-free biochemical quantitative phase imaging with mid-infrared photothermal effect," Optica **7**(4), 359–366 (2020).
33. K. Toda, M. Tamamitsu, and T. Ideguchi, "Adaptive dynamic range shift (ADRIFT) quantitative phase imaging," Light: Sci. Appl. **10**(1), 1 (2021).
34. C. Yurdakul, H. Zong, Y. Bai, J.-X. Cheng, and M. S. Ünlü, "Bond-selective interferometric scattering microscopy," J. Phys. D: Appl. Phys. **54**(36), 364002 (2021).
35. Y. Zhang, H. Zong, C. Zong, Y. Tan, M. Zhang, Y. Zhan, and J.-X. Cheng, "Fluorescence-Detected Mid-Infrared Photothermal Microscopy," J. Am. Chem. Soc. **143**(30), 11490–11499 (2021).
36. H. Zong, C. Yurdakul, Y. Bai, M. Zhang, M. S. Unlu, and J.-X. Cheng, "Background-suppressed high-throughput mid-infrared photothermal microscopy via pupil engineering," ACS Photonics **8**(11), 3323–3336 (2021).
37. J. Zhao, A. Matlock, H. Zhu, Z. Song, J. Zhu, B. Wang, F. Chen, Y. Zhan, Z. Chen, Y. Xu, X. Lin, L. Tian, and J.-X. Cheng, "Bond-selective intensity diffraction tomography," Nat. Commun. **13**(1), 7767 (2022).
38. Q. Xia, Z. Guo, H. Zong, S. Seitz, C. Yurdakul, M. S. Ünlü, L. Wang, J. H. Connor, and J.-X. Cheng, "Single virus fingerprinting by widefield interferometric defocus-enhanced mid-infrared photothermal microscopy," Nat. Commun. **14**(1), 6655 (2023).
39. Y. Bai, J. Yin, and J.-X. Cheng, "Bond-selective imaging by optically sensing the mid-infrared photothermal effect," Sci. Adv. **7**(20), eabg1559 (2021).
40. Q. Xia, J. Yin, Z. Guo, and J.-X. Cheng, "Mid-Infrared Photothermal Microscopy: Principle, Instrumentation, and Applications," J. Phys. Chem. B **126**(43), 8597–8613 (2022).
41. J. F. De Boer, C. K. Hitzenberger, and Y. Yasuno, "Polarization sensitive optical coherence tomography–a review," Biomed. Opt. Express **8**(3), 1838–1873 (2017).
42. H. S. Nam and H. Yoo, "Spectroscopic optical coherence tomography: A review of concepts and biomedical applications," Appl. Spectrosc. Rev. **53**(2-4), 91–111 (2018).
43. T. Wang, T. Pfeiffer, M. Wu, W. Wieser, G. Amenta, W. Draxinger, A. F. Van Der Steen, R. Huber, and G. Van Soest, "Thermo-elastic optical coherence tomography," Opt. Lett. **42**(17), 3466–3469 (2017).
44. A. D. Deen, H. M. Van Beusekom, T. Pfeiffer, M. Stam, D. De Kleijn, J. Wentzel, R. Huber, A. F. Van Der Steen, G. Van Soest, and T. Wang, "Spectroscopic thermo-elastic optical coherence tomography for tissue characterization," Biomed. Opt. Express **13**(11), 1430–1446 (2022).
45. D. C. Adler, S.-W. Huang, R. Huber, and J. G. Fujimoto, "Photothermal detection of gold nanoparticles using phase-sensitive optical coherence tomography," Opt. Express **16**(7), 4376–4393 (2008).
46. G. Goetz, T. Ling, T. Gupta, S. Kang, J. Wang, P. D. Gregory, B. H. Park, and D. Palanker, "Interferometric mapping of material properties using thermal perturbation," Proc. Natl. Acad. Sci. U. S. A. **115**(11), E2499–E2508 (2018).
47. M. Lapierre-Landry, A. Y. Gordon, J. S. Penn, and M. C. Skala, "In vivo photothermal optical coherence tomography of endogenous and exogenous contrast agents in the eye," Sci. Rep. **7**(1), 9228 (2017).
48. M. Lapierre-Landry, A. L. Huckenpahler, B. A. Link, R. F. Collery, J. Carroll, and M. C. Skala, "Imaging melanin distribution in the zebrafish retina using photothermal optical coherence tomography," Trans. Vis. Sci. Tech. **7**(5), 4 (2018).
49. M. Lapierre-Landry, T. B. Connor, J. Carroll, Y. K. Tao, and M. C. Skala, "Photothermal optical coherence tomography of indocyanine green in ex vivo eyes," Opt. Lett. **43**(11), 2470–2473 (2018).
50. J. M. Tucker-Schwartz, T. Hong, D. C. Colvin, Y. Xu, and M. C. Skala, "Dual-modality photothermal optical coherence tomography and magnetic-resonance imaging of carbon nanotubes," Opt. Lett. **37**(5), 872–874 (2012).
51. Y. Jung, R. Reif, Y. Zeng, and R. K. Wang, "Three-dimensional high-resolution imaging of gold nanorods uptake in sentinel lymph nodes," Nano Lett. **11**(7), 2938–2943 (2011).
52. A. S. Paranjape, R. Kuranov, S. Baranov, L. L. Ma, J. W. Villard, T. Wang, K. V. Sokolov, M. D. Feldman, K. P. Johnston, and T. E. Milner, "Depth resolved photothermal OCT detection of macrophages in tissue using nanorose," Biomed. Opt. Express **1**(1), 2–16 (2010).

Optics EXPRESS

53. C. Zhou, T.-H. Tsai, D. C. Adler, H.-C. Lee, D. W. Cohen, A. Mondelblatt, Y. Wang, J. L. Connolly, and J. G. Fujimoto, "Photothermal optical coherence tomography in ex vivo human breast tissues using gold nanoshells," Opt. Lett. **35**(5), 700–702 (2010).
54. M. C. Skala, M. J. Crow, A. Wax, and J. A. Izatt, "Photothermal optical coherence tomography of epidermal growth factor receptor in live cells using immunotargeted gold nanospheres," Nano Lett. **8**(10), 3461–3467 (2008).
55. M. H. Salimi, M. Villiger, and N. Tabatabaei, "Transient-mode photothermal optical coherence tomography," Opt. Lett. **46**(22), 5703–5706 (2021).
56. M. Salimi, M. Villiger, and N. Tabatabaei, "Effects of lipid composition on photothermal optical coherence tomography signals," J. Biomed. Opt. **25**(12), 120501 (2020).
57. I. Zorin, P. Gattinger, M. Brandstetter, and B. Heise, "Dual-band infrared optical coherence tomography using a single supercontinuum source," Opt. Express **28**(6), 7858–7874 (2020).
58. E. O. Potma, D. Knez, Y. Chen, Y. Davydova, A. Durkin, A. Fast, M. Balu, B. Norton-Baker, R. W. Martin, and T. Baldacchini, "Rapid chemically selective 3D imaging in the mid-infrared," Optica **8**(7), 995–1002 (2021).
59. V. Mazlin, P. Xiao, J. Scholler, K. Irsch, K. Grieve, M. Fink, and A. C. Boccara, "Real-time non-contact cellular imaging and angiography of human cornea and limbus with common-path full-field/SD OCT," Nat. Commun. **11**(1), 1868 (2020).
60. A. Dubois, G. Moneron, K. Grieve, and A. C. Boccara, "High-resolution three-dimensional imaging inside biological media using white-light interference microscopy," in *European Conference on Biomedical Optics*, (Optica Publishing Group, 2003), 5140–5143.
61. M. Maggioni, V. Katkovnik, K. Egiazarian, and A. Foi, "Nonlocal transform-domain filter for volumetric data denoising and reconstruction," IEEE Trans. on Image Process. **22**(1), 119–133 (2013).
62. L. P. DeFlores and A. Tokmakoff, "Water Penetration into Protein Secondary Structure Revealed by Hydrogen–Deuterium Exchange Two-Dimensional Infrared Spectroscopy," J. Am. Chem. Soc. **128**(51), 16520–16521 (2006).
63. G. Cakmak, L. M. Miller, F. Zorlu, and F. Severcan, "Amifostine, a radioprotectant agent, protects rat brain tissue lipids against ionizing radiation induced damage: an FTIR microspectroscopic imaging study," Arch. Biochem. Biophys. **520**(2), 67–73 (2012).
64. M. A. Pleitez, O. Hertzberg, A. Bauer, T. Lieblein, M. Glasmacher, H. Tholl, and W. Mäntele, "Infrared reflectometry of skin: Analysis of backscattered light from different skin layers," Spectrochim. Acta, Part A **184**, 220–227 (2017).
65. F. Fereidouni, A. D. Mitra, S. Demos, and R. Levenson, "Microscopy with UV Surface Excitation (MUSE) for slide-free histology and pathology imaging," in *Optical Biopsy XIII: Toward Real-Time Spectroscopic Imaging and Diagnosis*, (SPIE, 2015), 46–51.